On the Reduction of the Reconstruction Bias in Synthetic Aperture Imaging Radiometry (Corrected)*

Eric Anterrieu, *Member, IEEE*

***Abstract*—Synthetic aperture imaging radiometers (SAIRs) are powerful instruments for high-resolution observation of planetary surfaces at low microwave frequencies. This paper is concerned with the reconstruction of radiometric brightness temperature maps from SAIR interferometric measurements. Even in the absence of modeling errors and radiometric noise, a systematic error, or bias, has been observed in the reconstructed maps. The origin of this bias is analyzed and an efficient solution is proposed for reducing it. The core reconstruction procedure is not changed, and no additional measurements are needed. Throughout the scientific rationale, particular emphasis is laid on numerical simulations carried out for the Soil Moisture and Ocean Salinity space mission, a project led by the European Space Agency and devoted to the remote sensing of soil moisture and ocean salinity from a low-orbit platform.**

***Index Terms*—Aperture synthesis, imaging radiometry, inverse problem, reconstruction bias, regularization.**

I. Introduction

THE two-dimensional L-band interferometer Microwave Imaging Radiometer by Aperture Synthesis (MIRAS) is the single payload of the Soil Moisture and Ocean Salinity (SMOS) space mission led by the European Space Agency [1], [2]. The problem of retrieving the radiometric temperature distribution of a scene under observation from interferometric data has been widely addressed [3]–[5], and the errors that may affect the reconstructed maps have been identified [6] and studied in depth [7], [8]. A linear algebra framework has been given to this problem [9], [10] showing that it has to be regularized in order to provide a unique and stable solution [10], [11].

This paper is devoted to the systematic error, or bias, which has been observed in the reconstructed maps, even in the absence of modeling errors and radiometric noise [10]. Removing such biases is an important issue, as systematic errors as small as 0.1 K may induce a 0.2 to 0.3 PSU error in the retrieved sea surface salinity. The modeling of the instrument and a regularized reconstruction procedure are briefly recalled in Sections II and III. The origins of the bias are addressed in Section IV. Two components are analyzed: the first one is related to the antenna voltage pattern of the reference radiometer [12], while the second one depends on the temperature contents in the aliased regions of the observed scene. Section V describes an approach for reducing this bias. New *a priori* information is added to the regularized reconstruction procedure without the aid of any additional measurement. Numerical simulations conducted within the frame of the SMOS project are the basis of the analysis and the results presented in Sections IV and V.

II. Instrument Modeling

Synthetic aperture imaging radiometers (SAIRs) devoted to Earth observation measure the correlation between the signals collected by pairs of spatially separated antennas A_k and A_l which have overlapping fields of view, yielding samples of the visibility function $V(\mathbf{u})$, also termed complex visibilities [13], of the brightness temperature map $T(\boldsymbol{\xi})$ of the observed scene. The relationship between $V(\mathbf{u})$ and $T(\boldsymbol{\xi})$ [14] has been recently revisited in order to take into account mutual effects of close antennas [15]. It is now given by

$$V(\mathbf{u}_{kl}) \propto \frac{1}{\sqrt{\Omega_k \Omega_l}} \iint\limits_{\|\boldsymbol{\xi}\|\leq 1} F_k(\boldsymbol{\xi}) \overline{F}_l(\boldsymbol{\xi}) \frac{T(\boldsymbol{\xi}) - T_{\mathrm{rec}}}{\sqrt{1-\|\boldsymbol{\xi}\|^2}} \times \widetilde{r}_{kl}\left(\frac{-\mathbf{u}_{kl}\boldsymbol{\xi}}{f_{\mathrm{o}}}\right) e^{-2j\pi \mathbf{u}_{kl}\boldsymbol{\xi}} d\boldsymbol{\xi} \quad (1)$$

where $\mathbf{u}_{kl}$ is the spatial frequency associated with the two antennas A_k and A_l (namely, the spacing $\mathbf{d}_{kl}$ between the antennas normalized to the central wavelength of observation λ_{o}), the components $\xi_1 = \sin\theta\cos\phi$ and $\xi_2 = \sin\theta\sin\phi$ of the angular position variable $\boldsymbol{\xi}$ are direction cosines (θ and ϕ are the traditional spherical coordinates), T_{rec} is the physical temperature of the receivers, $F_k(\boldsymbol{\xi})$ and $F_l(\boldsymbol{\xi})$ are the normalized voltage patterns of the two antennas A_k and A_l with equivalent solid angles Ω_k and Ω_l (the overbar indicates the complex conjugate), $\widetilde{r}_{kl}(t)$ is the so-called fringe-wash function which accounts for spatial decorrelation effects, $t = \mathbf{u}_{kl}\boldsymbol{\xi}/f_{\mathrm{o}}$ is the spatial delay and $f_{\mathrm{o}} = c/\lambda_{\mathrm{o}}$ is the central frequency of observation.

Denoting by ℓ the number of antennas of the interferometric array, the number of complex visibilities (i.e., the number of baselines $\mathbf{d}_{kl}$) provided by the interferometer is equal to $n_v = \ell(\ell-1)/2$ when accounting for the Hermitian property of (1). However, the list of spatial frequencies $\mathbf{u}_{kl}$ is not necessarily nonredundant since two different pairs of antennas may lead to the same spatial frequency [16].

*Corrected. This paper first appeared in the *IEEE Transactions on Geoscience and Remote Sensing, vol. 45, no. 3, pp. 592–601, March 2007*. Due to a processing error by the publisher, Fig. 1 did not print properly, thus affecting the readability of the paper. This revised version replaces the previous version. We apologize for the error.

Manuscript received May 5, 2006; revised August 28, 2006. This work was supported in part by the Centre National de la Recherche Scientifique and in part by the European Space Agency within the framework of the Expert Support Laboratories (ESL) activities while under contract with DEIMOS ENGENHARIA (Grant SMOSP2-DME-LAT-0805).

The author is with the Laboratoire d'Astrophysique de Toulouse–Tarbes (LATT), 31400 Toulouse, France (e-mail: Eric.Anterrieu@ast.obs-mip.fr).

Digital Object Identifier 10.1109/TGRS.2007.894270

Since SAIR have limited physical dimensions, the spatial frequencies $\mathbf{u}_{kl}$ sampled by an interferometer are confined to a limited region of the Fourier domain: the so-called experimental frequency coverage H [17]. In the case of MIRAS, a Y-shaped array fitted with equally spaced antennas has been selected. Consequently, the visibility samples are obtained from raw data inside a star-shaped window over an hexagonally sampled grid $\mathbb{G}_u$ in the Fourier domain [1].

Finally, for computational purposes, numerical integration is used to represent the integral (1) as a summation over n^2 integrand samples, here the n^2 pixels of the spatial grid $\mathbb{G}_\xi$ which is the dual grid of $\mathbb{G}_u$. The number of pixels in the grids $\mathbb{G}_u$ and $\mathbb{G}_\xi$ has to be chosen in such a way that the Shannon criterion is satisfied and the numerical quadrature is sufficiently accurate [10].

III. Reconstruction Procedure

A new regularized approach has recently been proposed, and selected by the European Space Agency for implementation in the ground segment prototype, for retrieving a unique and stable estimate T_r of the radiometric temperature distribution T of a scene under observation from complex visibilities V [10]. Like many other reconstruction procedures, this method makes use of the modeling operator (or matrix) $\mathbf{G}$ which is the discrete linear operator from the object space E into the data space F describing the basic relation (1). It has been shown that this approach provides the best estimate T_r inasmuch as all the available information is taken into account in the (regularized) inversion [11]. The information required to build the $\mathbf{G}$ matrix is not relevant for this paper since the origin of the reconstruction bias is not linked to unknown modeling errors and it appears even when the modeling $\mathbf{G}$ matrix is perfectly known [10].

Referring to a physical concept, namely the limited resolution of SAIR, this regularized approach finds the temperature map T_r which has its Fourier transform confined to the experimental frequency coverage H. This band-limited solution realizes the minimum of the constrained optimization problem

$$\begin{cases} \min\limits_{T\in E} \|V - \mathbf{G}T\|_F^2 \\ (\mathbf{I} - \mathbf{P}_H)T = 0 \end{cases} \tag{2}$$

where $\mathbf{P}_H = \mathbf{U}^*\mathbf{Z}\mathbf{Z}^*\mathbf{U}$ is the projector onto the subspace $\mathcal{E}$ (of the object space E) of the H band-limited functions, $\mathbf{U}$ is the Fourier transform operator, and $\mathbf{Z}$ is the zero-padding operator beyond H. The unique solution of (2) is given by

$$T_\mathrm{r} = \mathbf{U}^*\mathbf{Z}\mathbf{A}^+V \tag{3}$$

where $\mathbf{A}^+ = (\mathbf{A}^*\mathbf{A})^{-1}\mathbf{A}^*$ is the More–Penrose pseudoinverse of the rectangular matrix $\mathbf{A} = \mathbf{G}\mathbf{U}^*\mathbf{Z}$.

In order to filter out the Gibbs effects due to the sharp frequency cutoff associated to the limited experimental frequency coverage H, T_r is damped by an appropriate windowing function W [18]

$$\mathcal{T}_\mathrm{r} = \mathbf{U}^*\widehat{\mathbf{W}}\mathbf{U}T_\mathrm{r} \tag{4}$$

where $\widehat{\mathbf{W}}$ is the diagonal matrix whose nonzero elements are the values of $\widehat{W}$ in H. As demonstrated and illustrated in [10], this map has to be compared to the temperature map to be reconstructed $\mathcal{T}_w = \mathbf{U}^*\widehat{\mathbf{W}}\mathbf{U}T$ and not to the original one T. Indeed, $\mathcal{T}_w$ is the map reconstructed with an "ideal" instrument (with identical antenna patterns and no fringe washing) and apodized with the same window W so that it is at the same spatial resolution as $\mathcal{T}_\mathrm{r}$ (whereas T is at a higher resolution and could not be compared to $\mathcal{T}_\mathrm{r}$). The corresponding error map $\Delta\mathcal{T}_\mathrm{r} = \mathcal{T}_\mathrm{r} - \mathcal{T}_w$ is characterized with its mean $\overline{\Delta\mathcal{T}}_\mathrm{r}$, or bias, and its standard deviation $\sigma_{\Delta\mathcal{T}_\mathrm{r}}$

$$\begin{aligned} \overline{\Delta\mathcal{T}}_\mathrm{r} &= \sum_{\mathrm{AFOV}} \Delta\mathcal{T}_\mathrm{r}(\boldsymbol{\xi})/n_{\mathrm{AFOV}} \\ \sigma_{\Delta\mathcal{T}_\mathrm{r}} &= \sqrt{\sum_{\mathrm{AFOV}} (\Delta\mathcal{T}_\mathrm{r}(\boldsymbol{\xi}) - \overline{\Delta\mathcal{T}_\mathrm{r}})^2/n_{\mathrm{AFOV}}}. \end{aligned} \tag{5}$$

The instantaneous field of view of MIRAS being subject to Earth and sky aliasing because of the antenna spacing of the Y-shaped interferometric array [1], [2], both quantities $\overline{\Delta\mathcal{T}}_\mathrm{r}$ and $\sigma_{\Delta\mathcal{T}_\mathrm{r}}$ are computed in the alias-free field of view (AFOV) by summing the values of the error map over the n_{AFOV} pixels belonging to this region of the synthesized field of view.

The results presented in the next sections are based on numerical simulations conducted within the frame of the SMOS project and with inputs from the SMOS End-to-End Performance Simulator (SEPS) [19]. All these simulations have been performed for a Y-shaped array equipped with $\ell = 69$ antennas. The number of available complex visibilities $V(\mathbf{u}_{kl})$ is equal to $n_v = 2346$, while there are only $n_f = 1395$ spatial frequencies in the star-shaped frequency coverage H. Only one reference radiometer consisting of an antenna element equipped with an accurately calibrated receiver has been added to the interferometric array in order to measure the visibility function for the zero spacing $V(\mathbf{0})$. The dimension of the sampling grids $\mathbb{G}_\mathrm{u}$ and $\mathbb{G}_\xi$ has been fixed to $n^2 = 128 \times 128$. The size of the real-valued matrices $\mathbf{G}$ and $\mathbf{A}$ are therefore $(2n_v+1)\times n^2 = 4693 \times 16\,384$ and $(2n_v+1)\times(2n_f+1) = 4693 \times 2791$, respectively.

IV. Origin of the Reconstruction Bias

Referring back to (5), the reconstruction bias is only one component of the systematic reconstruction error which has been observed even in the absence of modeling errors and radiometric noise [10]. It has been attributed to the high-frequencies components of the observed scene which contribute to the complex visibilities while the instrument provides only the capability to retrieve a band-limited brightness temperature map. However, as illustrated in Fig. 1 with the spatial frequency filtering characteristics of MIRAS, the instrument is not sensitive to spatial frequencies that are higher than its maximum baseline. Indeed, this basic property is revealed with the aid of numerical simulations conducted for an input

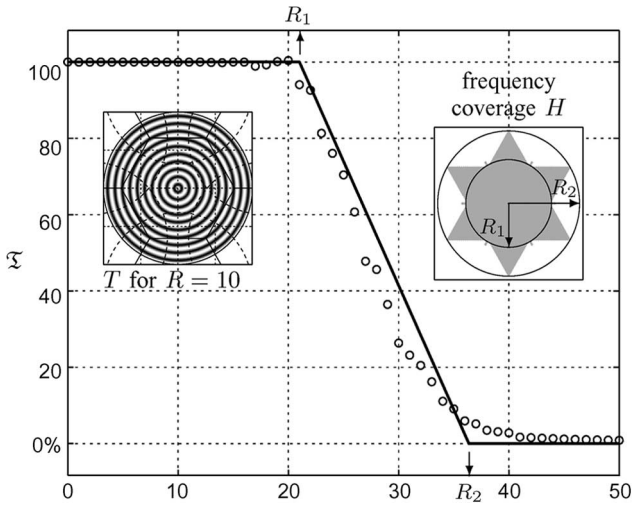

Fig. 1. Variations of the transmission factor $\mathfrak{T}$ of MIRAS with the spatial frequency R of an input cosine wave of the form $T = \cos(2\pi R\sqrt{\xi_1^2 + \xi_2^2})$: $\mathfrak{T}$ is defined as the ratio between the amplitude of the retrieved cosine wave T_r and that of the original one T, R is expressed with the same units the spatial frequencies $\mathbf{u}_{kl}$ are. Circles are results of numerical simulations, and the solid line curve is the expected behavior for an SAIR with such a star-shaped frequency coverage H with $R_1 = 21$ and $R_2 = \sqrt{3}R_1 \simeq 36.4$.

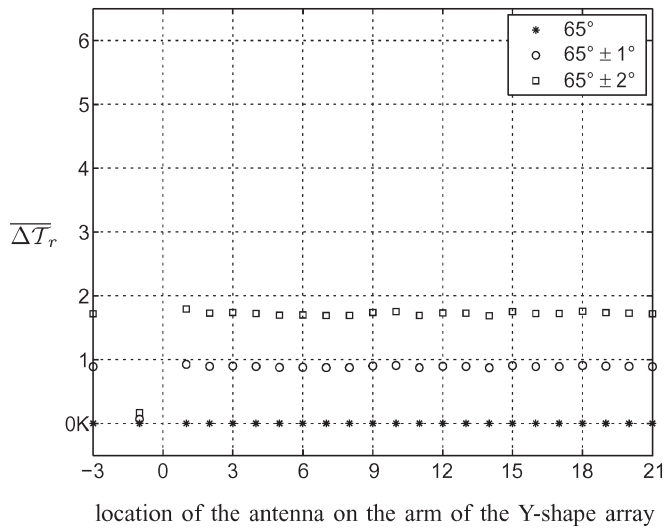

Fig. 2. Variations of the bias $\overline{\Delta T}_\mathrm{r}$ with the location of a particular antenna having its voltage pattern with the FWHM set to 65° while the 68 other antennas of MIRAS have equal voltage patterns with the FWHM set to 65° or different ones with their FWHM in the range $65° \pm 1°$ or $65° \pm 2°$. There are 21 front antennas and two back ones per arm. The reference antenna is one of the latter and is always located at coordinate -1 just behind the center of the Y.

cosine wave $T(\boldsymbol{\xi}) = \cos(2\pi R\sqrt{\xi_1^2 + \xi_2^2})$ with various spatial frequencies R in a range higher than the length of the maximum baseline and by computing the ratio $\mathfrak{T}$ between the amplitude of the retrieved cosine wave T_r and that of the original one T. According to the shape of the experimental frequency coverage H, the following behavior is expected (and actually observed) for this transmission factor: $\mathfrak{T} = 1$ below R_1 (the radius of the circle inscribed in H), $\mathfrak{T} = 0$ above R_2 (the radius of the circle circumscribed around H) and $\mathfrak{T}$ varies linearily from 1 down to 0 for $R_1 \leq R \leq R_2$. As a consequence, the reconstruction bias cannot be attributed to the high-frequencies components of the observed scene since they are filtered out by the instrument itself.

With regard to this band-limited imaging property, the situation of MIRAS is very similar to that of any interferometer in radio astronomy (such as the very large array [20], for example). In particular, the truncation of the experimental frequency coverage H is responsible for the standard deviation component of the systematic error because of the presence of the well-known Gibbs oscillations in the reconstructed maps. However, some specific features may be responsible for the systematic bias.

1) Due to the short spacing between the antennas, the synthesized field of view of MIRAS is much larger than with any interferometric array in radio astronomy. Since the antenna patterns are also wider than in radio astronomy, nonnegligible effects of individual antenna patterns should be taken into account.
2) In radio astronomy, typically observed fields have a background level close to zero whereas for the SMOS mission the average temperature of the Earth is not close to zero. Since the spacing and the geometry of the array are also responsible for Earth (and sky) aliases in the synthesized field of view, the influence of these regions could be very critical.

Consequently, the following two origins, or two components, of the reconstruction bias have been investigated:

1) an *instrument-dependent component*, which has revealed the key role played by the voltage pattern of the reference radiometer;
2) a *scene-dependent component*, which has shown the influence of the aliased regions of the observed scene.

Simulations have been performed in this section with very simple synthetic scenes in order to reveal these effects while in Section V other simulations have been conducted with more realistic scenes taken from the SEPS [19].

A. Instrument-Dependent Component

Simulations have been first conducted for an array with one particular antenna pattern having a full-width at half-maximum (FWHM) permanently set to 65° (i.e., close to the nominal MIRAS value), while the FWHM of the other antennas is also set to 65° or randomly distributed over $65° \pm 1°$ and $65° \pm 2°$. The observed scene is a very simple brightness temperature distribution T equal to 300 K over the Earth and 0 K elsewhere, so that the AFOV is also free from aliases from the sky. The variations of the bias $\overline{\Delta T}_\mathrm{r}$ with the location of a particular antenna on one arm of the Y-shape array are shown in Fig. 2. As expected, $\overline{\Delta T}_\mathrm{r}$ is equal to zero when all the antennas have the same voltage pattern (i.e., when the instrument is an ideal one). This is no longer the case when the antennas have different voltage patterns, except when the particular one plays the role of the reference antenna. It should be noted that in such a case the voltage pattern of the reference antenna is here equal to the average pattern of the other antennas of the array (whatever the spread of these patterns). For the other locations, the bias does not depend on the location of the particular antenna and is an increasing function of the disparity between the voltage patterns, at a rate here close to 1 K/°.

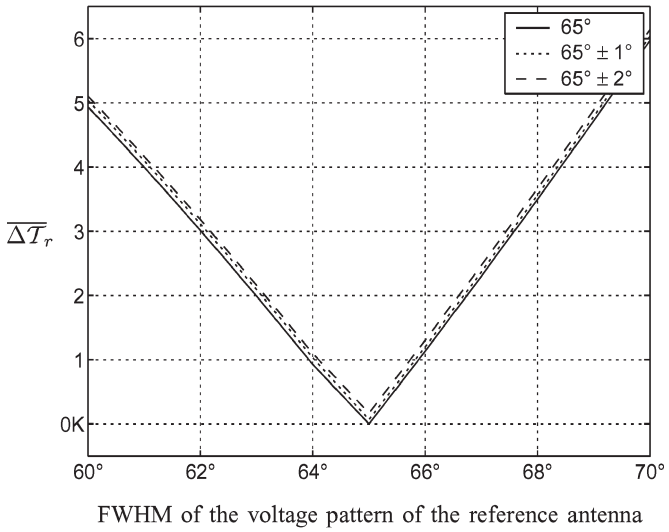

Fig. 3. Variations of the bias $\overline{\Delta T}_{\mathrm{r}}$ with the FWHM of the voltage pattern of the NIR. The 68 other antennas of MIRAS have equal voltage patterns with the FWHM set to 65° or different ones with their FWHM in the range $65^\circ \pm 1^\circ$ or $65^\circ \pm 2^\circ$.

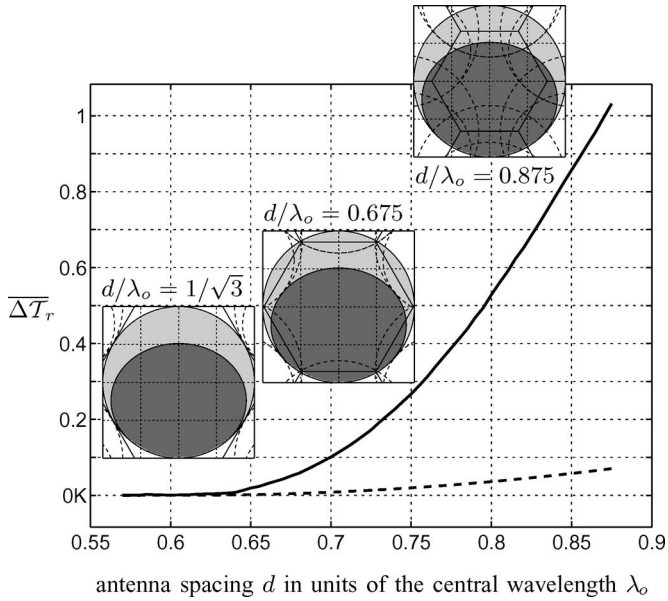

Fig. 4. Variations of the bias $\overline{\Delta T}_{\mathrm{r}}$ with the spacing d between the antennas for an instrument with different antenna patterns. For the dotted line curve, the pattern of the NIR is equal to the average of the other patterns, while for the solid curve it is not. Temperature maps are displayed for three typical values of d (dark gray is 300 K, and light gray is 0 K).

The same simulations have been repeated with the particular antenna having its voltage pattern now with the FWHM set to 70°, so that its pattern is no longer equal to the average pattern of the other antennas. Compared to the previous simulations, the result is almost identical except when the particular antenna plays the role of the reference antenna. Indeed, now the voltage pattern of the reference antenna differs significantly from the average pattern of the other antennas and consequently the bias is no longer equal to zero, but about 6 K. Moreover, in such a situation the value of $\overline{\Delta T}_{\mathrm{r}}$ is larger than any values obtained for the other locations occupied by the particular antenna and it does not depend on the spread between the voltage patterns.

Finally, shown in Fig. 3 are the variations of $\overline{\Delta T}_{\mathrm{r}}$ with the FWHM of the reference antenna while all the other antennas have voltage patterns, either with the same FWHM set to 65° or with different ones in the range $65^\circ \pm 1^\circ$ and $65^\circ \pm 2^\circ$. The value 65° for the FWHM of the reference antenna is clearly a minimum for the bias, which increases linearly with the absolute difference between the FWHM of the reference antenna and that of the average pattern of the other antennas. However, the obtained minimum is zero because a single varying parameter (the FWHM) has been used for modeling differencies between antenna patterns. When considering actual antennas, this will no longer be true and the same curve will exhibit a minimum larger than zero (see Section V-A).

One may wonder whether or not the conditions of the previous simulations are particular ones with respect, for example, to the extent of the synthesized field of view which is about 82.6° or with the one of the Earth seen from an altitude of 755 km which is 63.4°. Accordingly, the same simulations have been performed with different random distributions and with different values for the FWHM (in the range 50° to 80°) of each voltage pattern. The same behavior has been observed regarding the variations of the reconstruction bias with the location of an antenna with a particular voltage pattern (Fig. 2) or with the FWHM of the voltage pattern of the reference antenna (Fig. 3).

Accordingly, it can be inferred that the reference antenna plays a key role regarding the reconstruction bias because its measurement is directly linked to the average temperature of the scene. Surprisingly enough, for the bias to be minimal, it is not necessary that all the voltage patterns be the same. From the linear algebra point of view, the condition necessary and sufficient for minimizing the bias is that the voltage pattern of the reference antenna should be as close as possible (in the least-square sense) to the average pattern of every antenna of the interferometer, whatever the spread between their patterns.

B. Scene-Dependent Component

Coming back now to the inverse problem to be solved, i.e., find an estimate T_{r} of T consistent with the interferometric data $V = \mathbf{G}T$, the difficulty of the situation is coming from these regions of the observed scene T which are seen by each individual antenna but are aliased in the field of view synthesized by the instrument because of the spacing d between antennas (as demonstrated in [18], the extension of this hexagonal field of view in the direction cosines frame attached to the instrument is equal to $2\lambda_{\mathrm{o}}/\sqrt{3}d \simeq 1.32$ because $d = 0.875\lambda_{\mathrm{o}}$). Since the contribution of these regions to the complex visibilities V cannot be subtracted prior to inversion (because the temperature distribution within these regions is not known), this term is an input error which propagates through the reconstruction process. The corresponding reconstruction error is a bias rather than a random contribution because this contribution does not exhibit a random distribution and is scene dependent.

The level of this bias should therefore grow with the spacing between the antennas since the extent of the aliased regions is an increasing function of d. This is illustrated by the results of numerical simulations shown in Fig. 4 for a simple brightness

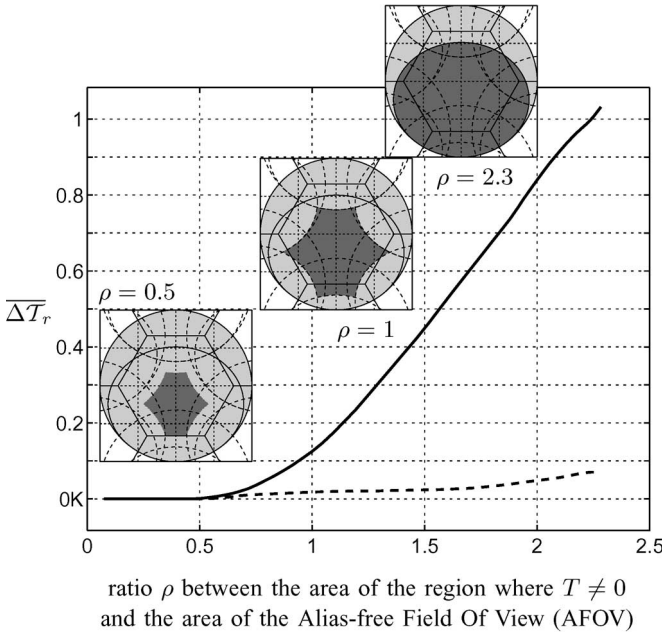

Fig. 5. Variations of the bias $\overline{\Delta T}_{\mathrm{r}}$ with the ratio ρ between the area of the region where $T \neq 0$ and the area of the AFOV for an instrument with different antenna patterns. For the dotted line curve, the pattern of the NIR is equal to the average of the other patterns, while for the solid curve it is not. Temperature maps are displayed for three typical values of ρ (dark gray is 300 K, and light gray is 0 K).

temperature map T equal to 300 K over the Earth and 0 K elsewhere, so that the AFOV is always free from aliases from the sky. It should be noted that a nonaverage pattern for the NIR is an aggravating condition for the level of the bias.

The spacing between the antennas of MIRAS has already been chosen and frozen to the value $d = 0.875\lambda_{\mathrm{o}}$. According to the previous figure, a bias coming from aliased regions should therefore be expected. The level of this bias should depend on the amount of the folding energy coming from these regions of the observed scene which are aliased in the synthesized field of view. This is illustrated by the results of numerical simulations shown in Fig. 5 for a simple brightness temperature map T equal to 300 K over a region of the Earth which is widening from the vicinity of the subsatellite point up to the whole Earth horizon, and to 0 K elsewhere so that influence of the aliases is controlled by the extent of the region where T is equal to 300 K. As expected, two domains clearly appear on the graph showing the variations of $\overline{\Delta T}_{\mathrm{r}}$ with the ratio ρ between the numbers of pixels (or the areas of the regions) where $T \neq 0$ K and in the AFOV. For $\rho = 1$, the 0 K/300 K transition coincides with the geometrical limits of the AFOV. When $\rho < 1$, i.e., when the region where $T = 300$ K does not extend beyond the AFOV, the bias is close to zero. On the other hand, when $\rho > 1$, i.e., when some regions where $T = 300$ K are aliased, the bias increases steeply. The vicinity of $\rho = 1$ is a transition region in which the bias is not exactly zero because the transition from the AFOV to aliases is not as sharp as suggested by a geometrical point of view. Indeed, the windowing function W introduced for smoothing the Gibbs oscillations is also responsible for smoothing the 0 K/300 K transition with some leakage effect. Here, again, it should be noted that a nonaverage pattern for the NIR is an aggravating condition for the level of the bias.

Accordingly, it can be inferred that this scene-dependent component of the bias cannot be reduced by the hardware, except by reducing the spacing between the antennas. Only a numerical approach can reduce this bias by removing, as far as possible, the contribution of the aliased regions of the observed scene from the visibility measurements prior to inversion.

V. Reduction of the Reconstruction Bias

Two approaches are presented here for reducing the scene-dependent component of the bias. The driving idea is to subtract, from the complex visibilities V, the contribution $\widetilde{V}$ of a brightness temperature distribution $\widetilde{T}$, which is "as close as possible" to the observed scene T. More precisely, instead of solving the inverse problem $V = \mathbf{G}T$ in the least-square sense with the regularized approach (2), the differential system $\delta V = \mathbf{G}\delta T$ is solved for δT with $\delta V = V - \widetilde{V}$ and $\widetilde{V} = \mathbf{G}\widetilde{T}$. The same regularized inversion is used and the temperature map $\widetilde{T}$ is added to the solution δT_{r} thus obtained, so that the solution (3) now writes

$$T_{\mathrm{r}} = \mathbf{U}^{*}\mathbf{Z}\mathbf{A}^{+}(V - \mathbf{G}\widetilde{T}) + \widetilde{T}. \tag{6}$$

Of course, the artificial scene $\widetilde{T}$ should be synthesized without any additional measurements. Moreover, it should contain "as far as possible" the aliased temperature distribution responsible for the scene-dependent component of the bias so that, ideally, the regularized inversion procedure is not perturbed by aliasing.

Numerical simulations have been performed with a set of antenna voltage patterns taken from the SEPS [19] which have been randomly distributed over the simulated instrument so that any of these voltage patterns could play the role of the reference antenna. Five different brightness temperature distributions, also taken from the SEPS [19], have been used for these simulations. The corresponding maps are represented for the X and Y polarizations in Fig. 6 (T_X and T_Y brightness temperatures are combinations of horizontal and vertical polarizations over the Earth [21]). The corresponding reconstruction biases and standard deviations, before any correction, are given in Table I for the best and the worst situations with regard to the voltage pattern playing the role of the reference antenna (the best being when the voltage pattern of the reference antenna is close to the average pattern of the other antennas, the worst being when it is far from this average pattern). The level and the location of sharp details (such as coastlines, islands, lakes, etc.) as well as the steepness of the Earth/sky transition which varies from one scene to another and also from one polarization to another for the same scene (see [22, App. 2]) are responsible for the notable differences observed in Table I. For example, the reconstruction errors for the "Pacific" and (to a lesser extent) "Africa" scenes are lowest mainly because the transition between Earth and cold sky is smooth, as ocean radiometric temperatures near the horizon are comparately cool. This is quite the contrary for the other scenes which have high-level Earth/sky transition and/or sharp details. The voltage pattern

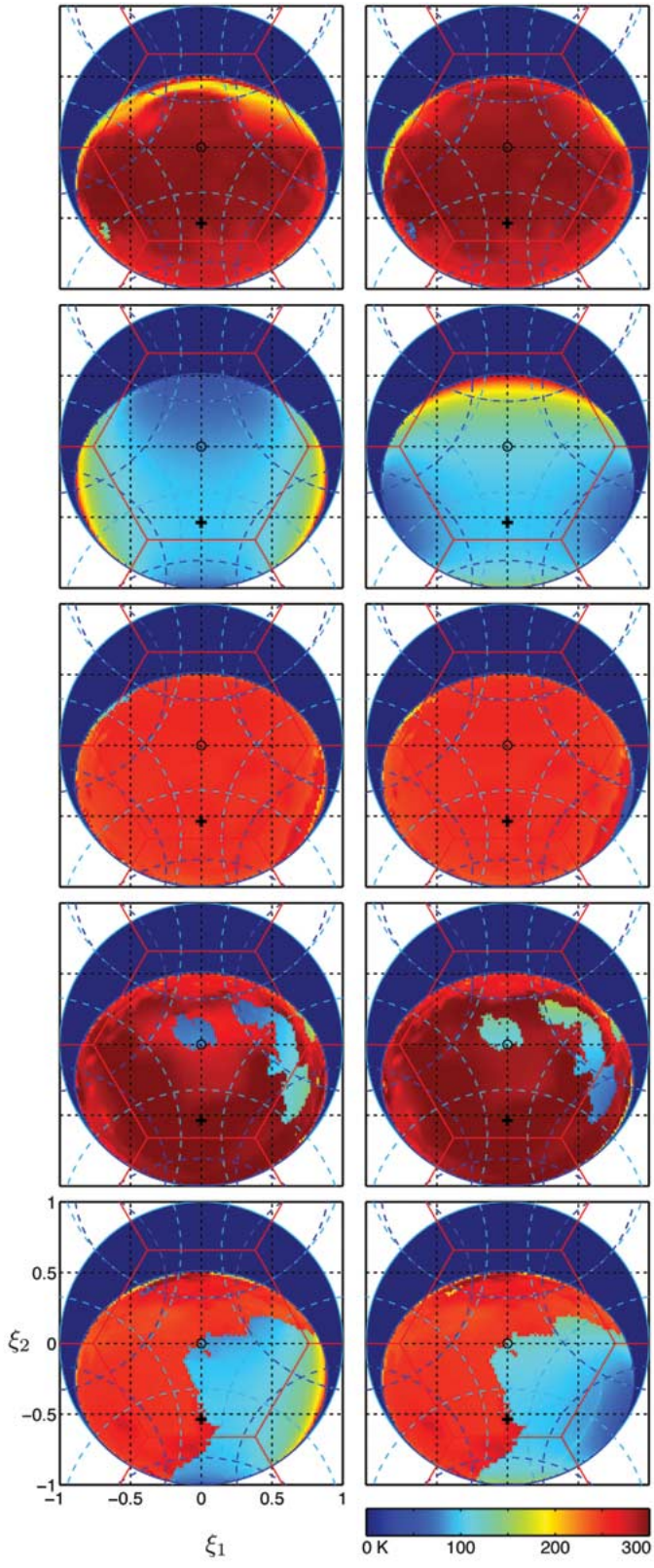

Fig. 6. Five test scenes used for the numerical simulations in (left) X and (right) Y polarizations in the frame attached to the instrument (west is pointing to the right). From top to bottom, they are named Sahara, Pacific, Europe, Caspian, and Africa.

of the antenna assigned to the reference radiometer has also an impact since the condition given at the end of Section IV-A proves to be better satisfied for the Y polarization than for the X one since the bias corresponding to the best situation is often smaller in Y polarization.

TABLE I
RECONSTRUCTION ERROR BEFORE CORRECTION

scene (see Fig. 6)		$\overline{\Delta\mathcal{T}_r}$ best / worst	$\sigma_{\Delta\mathcal{T}_r}$ best / worst
Africa	T_X	0.48 K 2.83 K	2.10 K 2.41 K
	T_Y	0.25 K 3.61 K	2.05 K 2.28 K
Caspian	T_X	0.45 K 4.17 K	3.01 K 3.49 K
	T_Y	0.47 K 5.66 K	3.01 K 3.26 K
Europe	T_X	0.47 K 3.85 K	2.55 K 2.95 K
	T_Y	0.05 K 4.34 K	2.89 K 3.08 K
Pacific	T_X	0.22 K 1.73 K	1.33 K 1.48 K
	T_Y	0.04 K 1.67 K	1.20 K 1.27 K
Sahara	T_X	0.50 K 4.44 K	2.85 K 3.31 K
	T_Y	0.15 K 4.96 K	3.24 K 3.45 K

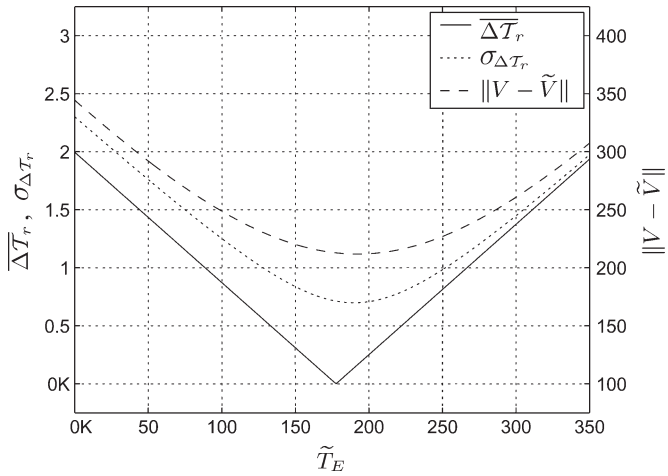

Fig. 7. Variations of the bias $\overline{\Delta\mathcal{T}}_{\mathrm{r}}$, the standard deviation $\sigma_{\Delta\mathcal{T}_{\mathrm{r}}}$ and the quadratic error $\|V-\widetilde{V}\|$ with $\widetilde{T}_{\mathrm{E}}$ ($\widetilde{T}_{\mathrm{S}}$ being equal to 3.7 K) for a simulation made with the "Africa" scene in X polarization.

A. Simplest Approach

A first approach for reducing the scene-dependent component of the bias is to subtract, from the complex visibilities V, the contribution $\widetilde{V}$ of a brightness temperature distribution $\widetilde{T}$ made of a constant temperature $\widetilde{T}_{\mathrm{E}}$ over the Earth and a constant temperature $\widetilde{T}_{\mathrm{S}}$ over the sky, so that the effect of the aliased regions should be reduced. Since $\widetilde{T}_{\mathrm{E}}$ and $\widetilde{T}_{\mathrm{S}}$ are not known, they are obtained through an optimization process which minimizes the quadratic error between the complex visibilities V and $\widetilde{V}$.

Shown in Fig. 7 is an example of the variations of the bias $\overline{\Delta\mathcal{T}}_{\mathrm{r}}$ and the standard deviation $\sigma_{\Delta\mathcal{T}_{\mathrm{r}}}$, together with those of the quadratic error $\|V-\widetilde{V}\|$, with the parameter $\widetilde{T}_{\mathrm{E}}$ ($\widetilde{T}_{\mathrm{S}}$ being equal to 3.7 K which is an average value when considering hydrogen line and continuum contributions in addition to the 2.7 K cosmic background) for a representative simulation made

TABLE II
RECONSTRUCTION ERROR AFTER $V(\mathbf{0})$ CORRECTION

scene (see Fig. 6)		$\overline{\Delta\mathcal{T}_r}$ best / worst	$\sigma_{\Delta\mathcal{T}_r}$ best / worst	$V(0)$
Africa	T_X	0.04 K 0.68 K	0.72 K 0.76 K	206.3 K 213.9 K
	T_Y	0.07 K 1.16 K	1.03 K 1.21 K	205.0 K 219.4 K
Caspian	T_X	0.07 K 0.46 K	0.65 K 0.69 K	274.7 K 286.3 K
	T_Y	0.08 K 0.84 K	0.97 K 1.12 K	280.8 K 305.0 K
Europe	T_X	0.03 K 0.31 K	0.37 K 0.47 K	265.7 K 275.6 K
	T_Y	0.01 K 0.39 K	0.36 K 0.56 K	262.3 K 285.5 K
Pacific	T_X	0.01 K 0.26 K	0.40 K 0.43 K	98.4 K 102.7 K
	T_Y	0.02 K 0.60 K	0.44 K 0.53 K	125.4 K 135.3 K
Sahara	T_X	0.06 K 0.40 K	0.51 K 0.61 K	294.4 K 306.1 K
	T_Y	0.09 K 0.52 K	0.54 K 0.77 K	298.9 K 325.5 K

TABLE III
RECONSTRUCTION ERROR AFTER SIMPLE CORRECTION

scene (see Fig. 6)		$\overline{\Delta\mathcal{T}_r}$ best / worst	$\sigma_{\Delta\mathcal{T}_r}$ best / worst	$\widetilde{T}_E$	$\widetilde{T}_S$
Africa	T_X	0.05 K 0.57 K	0.70 K 0.73 K	192.3 K 193.3 K	3.7 K
	T_Y	0.08 K 1.02 K	1.01 K 1.07 K	201.3 K 199.7 K	3.7 K
Caspian	T_X	0.03 K 1.04 K	0.84 K 0.96 K	230.1 K 231.2 K	3.7 K
	T_Y	0.01 K 1.39 K	0.87 K 0.91 K	254.8 K 253.0 K	3.7 K
Europe	T_X	0.001 K 0.07 K	0.31 K 0.32 K	254.8 K 254.8 K	3.7 K
	T_Y	0.003 K 0.17 K	0.32 K 0.33 K	255.0 K 254.8 K	3.7 K
Pacific	T_X	0.06 K 0.46 K	0.53 K 0.55 K	83.4 K 83.7 K	3.7 K
	T_Y	0.02 K 0.58 K	0.48 K 0.51 K	131.0 K 130.3 K	3.7 K
Sahara	T_X	0.04 K 0.18 K	0.46 K 0.47 K	284.1 K 284.2 K	3.7 K
	T_Y	0.01 K 0.29 K	0.51 K 0.52 K	293.4 K 292.9 K	3.7 K

with the test scene "Africa" in X polarization. In the absence of any correction, i.e., for $\widetilde{T}_{\mathrm{E}} = 0$ K, values computed for $\overline{\Delta\mathcal{T}}_{\mathrm{r}}$ and $\sigma_{\Delta\mathcal{T}_{\mathrm{r}}}$ are 2.00 and 2.30 K, respectively. However, a minimum can be found for both quantities since $\overline{\Delta\mathcal{T}}_{\mathrm{r}} = 0.0$ K and $\sigma_{\Delta\mathcal{T}_{\mathrm{r}}} = 0.70$ K when $\widetilde{T}_{\mathrm{E}} = 176.6$ K. This optimum cannot be reached because T_{r}, and therefore $\Delta\mathcal{T}_{\mathrm{r}}$, is not known. Only an approximate can be obtained through the minimization of the quadratic error $\|V - \widetilde{V}\|$ which also exhibits a minimum, but for $\widetilde{T}_{\mathrm{E}} = 192.3$ K. The corresponding values for the bias and the standard deviation are $\overline{\Delta\mathcal{T}}_{\mathrm{r}} = 0.16$ K and $\sigma_{\Delta\mathcal{T}_{\mathrm{r}}} = 0.71$ K. Consequently, in spite of different optimal values of $\widetilde{T}_{\mathrm{E}}$ for $\overline{\Delta\mathcal{T}}_{\mathrm{r}}$, $\sigma_{\Delta\mathcal{T}_{\mathrm{r}}}$ and $\|V - \widetilde{V}\|$, both the bias and the standard deviation have been significantly reduced. Finally, it has to be noted that the trivial approach $\widetilde{T}_{\mathrm{E}} = V(0)$, here equal to 213.9 K, leads to the values $\overline{\Delta\mathcal{T}}_{\mathrm{r}} = 0.41$ K and $\sigma_{\Delta\mathcal{T}_{\mathrm{r}}} = 0.75$ K.

The same behavior has been observed for the other scenes shown on Fig. 6. The final values of $\overline{\Delta\mathcal{T}}_{\mathrm{r}}$ and $\sigma_{\Delta\mathcal{T}_{\mathrm{r}}}$ are given in Table II after the low-cost correction with $\widetilde{T}_{\mathrm{E}} = V(0)$ and in Table III after the simple correction with optimized $\widetilde{T}_{\mathrm{E}}$ and $\widetilde{T}_{\mathrm{S}}$, again for the best and the worst situations with regard to the voltage pattern playing the role of the reference antenna, like given in Table I. Differences from one scene to another and between both polarizations, which were noticed before applying any correction, are still observed. However, both the bias and the standard deviation have been reduced significantly. While the overall results presented in Table III appear slightly better, both approaches lead to very close performances.

B. Adding More A Priori Information

The previous approach can be improved by introducing *a priori* information on the subtracted brightness temperature distribution $\widetilde{T}$ like coastlines or known variations with incidence angle [22]. The former information is here introduced with the aid of an ocean/land mask so that the brightness temperature distribution $\widetilde{T}$ is now equal to $\widetilde{T}_{\mathrm{O}}$ or $\widetilde{T}_{\mathrm{L}}$ over the Earth and to $\widetilde{T}_{\mathrm{S}}$ over the sky. Here, again, $\widetilde{T}_{\mathrm{O}}$, $\widetilde{T}_{\mathrm{L}}$, and $\widetilde{T}_{\mathrm{S}}$ are obtained through an optimization process which minimizes the quadratic error between the complex visibilities V and $\widetilde{V}$.

Shown in Fig. 8 is an example for the variations of the bias $\overline{\Delta\mathcal{T}}_{\mathrm{r}}$ and the standard deviation $\sigma_{\Delta\mathcal{T}_{\mathrm{r}}}$, together with those of the quadratic error $\|V - \widetilde{V}\|$, with the parameters $\widetilde{T}_{\mathrm{O}}$ and $\widetilde{T}_{\mathrm{L}}$ ($\widetilde{T}_{\mathrm{S}}$ being equal to 3.7 K) for the same representative simulation of Fig. 7. Without any correction, i.e., here for $\widetilde{T}_{\mathrm{O}} = \widetilde{T}_{\mathrm{L}} = 0$ K, $\overline{\Delta\mathcal{T}}_{\mathrm{r}} = 2.00$ K and $\sigma_{\Delta\mathcal{T}_{\mathrm{r}}} = 2.30$ K. Here, again, the true minimum values for both quantities, $\overline{\Delta\mathcal{T}}_{\mathrm{r}} = 0.0$ K and $\sigma_{\Delta\mathcal{T}_{\mathrm{r}}} = 0.36$ K, obtained when $\widetilde{T}_{\mathrm{O}} = 95$ K and $\widetilde{T}_{\mathrm{L}} = 250$ K, cannot be reached because T_{r}, and therefore $\Delta\mathcal{T}_{\mathrm{r}}$, is not known. Only approximate results can be obtained through minimizing the quadratic error $\|V - \widetilde{V}\|$ which also exhibits a minimum for $\widetilde{T}_{\mathrm{O}} = 94.9$ K and $\widetilde{T}_{\mathrm{L}} = 248.6$ K. The corresponding values found for the bias and the standard deviation are $\overline{\Delta\mathcal{T}}_{\mathrm{r}} = 0.02$ K and $\sigma_{\Delta\mathcal{T}_{\mathrm{r}}} = 0.43$ K. Consequently, in spite of different optimal values of $\widetilde{T}_{\mathrm{O}}$ and $\widetilde{T}_{\mathrm{L}}$ for $\overline{\Delta\mathcal{T}}_{\mathrm{r}}$, $\sigma_{\Delta\mathcal{T}_{\mathrm{r}}}$ and $\|V - \widetilde{V}\|$, both the bias and the standard deviation have been significantly reduced.

The same behavior has been observed with the other scenes for which an ocean/land mask is relevant (excluding therefore the "Europe" scene which is purely continental and the "Pacific" one which is pure ocean). The final values of $\overline{\Delta\mathcal{T}}_{\mathrm{r}}$ and $\sigma_{\Delta\mathcal{T}_{\mathrm{r}}}$ after this correction are given in Table IV. Here, again, both the bias and the standard deviation have been reduced significantly with respect to results presented in Tables II and III. The reconstructed images $\mathcal{T}_{\mathrm{r}}$ and the associated error maps $\Delta\mathcal{T}_{\mathrm{r}}$ obtained without any correction and those corresponding to Figs. 7 and 8 obtained with the two approaches presented in this section are shown in Fig. 9 for illustrating the visual effect of the reconstruction error and the performances of the two methods.

VI. CONCLUSION

The problem of the systematic error which is observed in brightness temperature maps reconstructed from visibility samples, even in the absence of modeling errors and radiometric

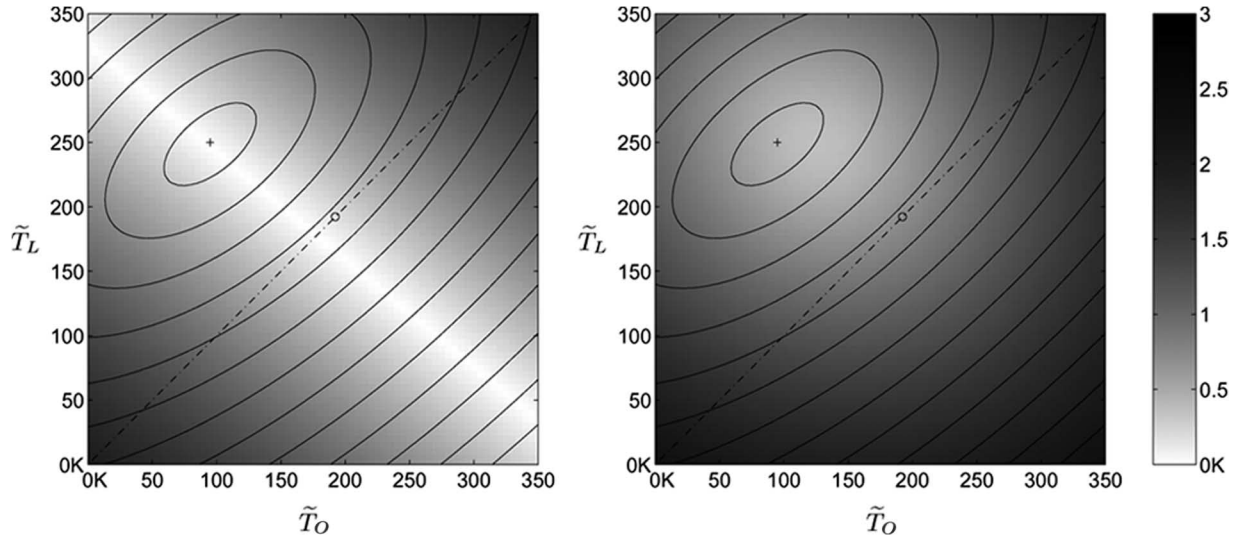

Fig. 8. Variations of the bias $\overline{\Delta T}_{\mathrm{r}}$ (left, gray tone image), the standard deviation $\sigma_{\Delta T_{\mathrm{r}}}$ (right, gray tone image), and the quadratic error $\|V - \widetilde{V}\|$ (contour levels) with $\widetilde{T}_{\mathrm{O}}$ and $\widetilde{T}_{\mathrm{L}}$ ($\widetilde{T}_{\mathrm{S}}$ being equal to 3.7 K) for a simulation made with the "Africa" scene in X polarization. The dotted line corresponds to the graph of Fig. 7 with $\widetilde{T}_{\mathrm{O}} = \widetilde{T}_{\mathrm{L}} = \widetilde{T}_{\mathrm{E}}$. The small circle is the location of the minimum for the previous approach with $\widetilde{T}_{\mathrm{E}}$ and $\widetilde{T}_{\mathrm{S}}$, while the cross is the location of the minimum for the actual approach with $\widetilde{T}_{\mathrm{S}}$, $\widetilde{T}_{\mathrm{O}}$, and $\widetilde{T}_{\mathrm{L}}$.

TABLE IV
RECONSTRUCTION ERROR AFTER IMPROVED CORRECTION

scene (see Fig. 6)		$\overline{\Delta T}_r$ best / worst	$\sigma_{\Delta T_r}$ best / worst	$\widetilde{T}_0$	$\widetilde{T}_L$	$\widetilde{T}_S$
Africa	T_X	0.01 K 0.44 K	0.43 K 0.45 K	94.9 K 95.0 K	248.6 K 248.6 K	3.7 K
	T_Y	0.03 K 0.22 K	0.29 K 0.30 K	108.7 K 108.5 K	255.4 K 255.2 K	3.7 K
Caspian	T_X	0.02 K 0.37 K	0.34 K 0.36 K	69.0 K 69.2 K	279.0 K 279.3 K	3.7 K
	T_Y	0.01 K 0.35 K	0.33 K 0.35 K	115.8 K 115.6 K	291.7 K 291.3 K	3.7 K
Sahara	T_X	0.01 K 0.15 K	0.46 K 0.47 K	0.02 K 0.03 K	284.3 K 284.5 K	3.7 K
	T_Y	0.01 K 0.23 K	0.44 K 0.45 K	143.9 K 143.0 K	293.1 K 292.8 K	3.7 K

noise, has been addressed. This systematic error has been characterized by its average (or bias) and standard deviation across the AFOV.

The origin of the bias has been studied and two major generating mechanisms have been investigated. The first one is related to the voltage pattern of the reference radiometer used for measuring the visibility function for the zero spacing. Since this measurement is related to the average temperature of the observed scene, the pattern of this antenna has a strong impact on the reconstruction bias. Due to manufacturing imperfections and the influence of locations in the interferometer, all the patterns cannot be expected to be identical. It has been shown that for this bias contribution to be minimal, the antenna with a pattern closest to the average one (in the least squares sense) should be assigned to the reference radiometer.

The second bias component depends on the temperature distribution in the aliased regions of the observed scene. These temperatures have been shown to contribute to the complex visibilities and they cannot be recovered because of the too large antenna spacing. Since the retrieved temperature map should be consistent with the data, these temperatures propagate through the reconstruction process like any input error. The corresponding bias cannot be reduced from the hardware: only a numerical approach introducing *a priori* information can reduce it by removing, as far as possible, the aliasing contribution from the complex visibilities prior to inversion. These two bias generating mechanisms do not operate independently: if the reference antenna pattern was strictly identical to the average pattern, there would be no reconstruction bias. As this ideal situation cannot be achieved, the second bias mechanism, triggered by aliasing, comes into play.

Finally, an efficient approach for reducing both the bias and the standard deviation of the systematic error has been presented and illustrated with numerical simulations. The driving idea is to subtract, from the complex visibilities, the contribution of an artificial brightness temperature distribution which is as close as possible to that of the observed scene without requiring any additional measurements and without any significant additional numerical cost for the reconstruction process.The first approach is a two-parameter linear optimization based on a flat target model for the Earth, while the second is based on a three-parameters model which takes advantage of the knowledge of the coastline and accounts for the difference between land and ocean so that the artificial brightness temperature distribution is closer to that of the observed scene. The latter approach might be improved with two additional parameters in order to take into account variations of the brightness temperature with the incidence angle. Other strategies, including iterative ones where the subtracted temperature distribution is updated after each reconstruction process, can also be implemented. However, they would be more time consuming and would require additional measurements (snapshots) over the observed scene. Furthermore, the proposed correction methods seem adequate to bring the reconstruction errors down to levels compatible with requirements over both land and ocean.

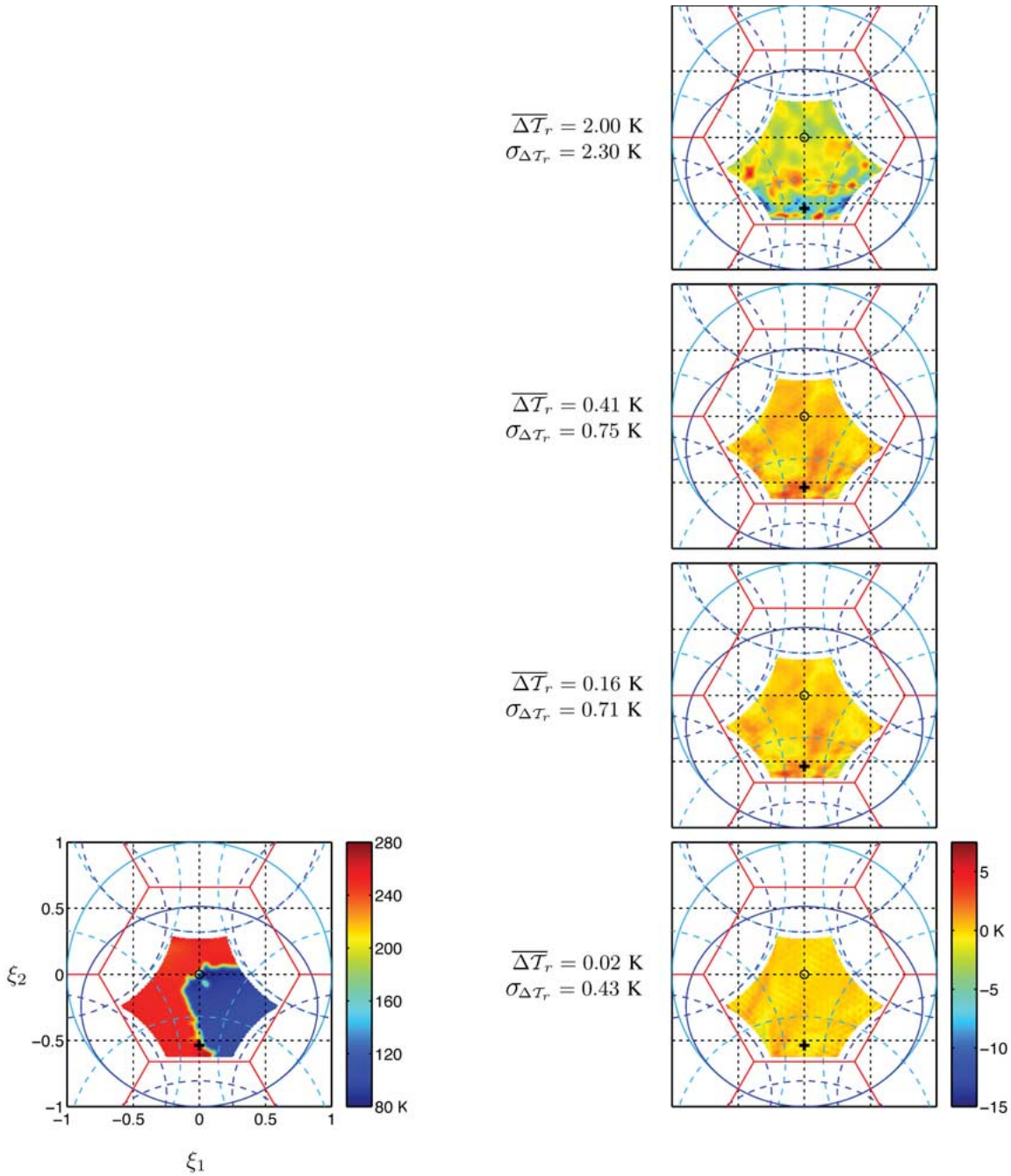

Fig. 9. Example of an image to be reconstructed $\mathcal{T}_w$ (left) with the "Africa" scene in X polarization and the corresponding error maps $\Delta\mathcal{T}_\mathrm{r} = \mathcal{T}_\mathrm{r} - \mathcal{T}_w$ (right, from top to bottom) without any correction, with the $V(\mathbf{0})$ low-cost correction, with the $\widetilde{T}_\mathrm{S}$ and $\widetilde{T}_\mathrm{E}$ simple model and with the $\widetilde{T}_\mathrm{S}$, $\widetilde{T}_\mathrm{O}$, and $\widetilde{T}_\mathrm{L}$ approach.

ACKNOWLEDGMENT

The author would like to thank P. Waldteufel (Service d'Aéronomie, Paris) and Y. Kerr (Centre d'Etudes Spatiales de la Biosphère Toulouse) for fruitful discussions and instructive comments throughout this paper. The author would also like to thank the anonymous referees whose comments have improved the quality of the original manuscript. Data processing was performed on a SUN Fire V20z server equipped with two single-core AMD Opteron processors (1-MB L2 cache, 8-GB memory) running Matlab 7 under 64-bit Red Hat Linux 3.4. The author is indebted to the Computer Support Group of Laboratoire d'Astrophysique de Toulouse–Tarbes for efficient assistance.

REFERENCES

[1] M. Martin-Neira, Y. Menard, J.-M. Goutoule, and U. Kraft, "MIRAS, A two-dimensional aperture synthesis radiometer," in *Proc. IGARSS*, Pasadena, CA, 1994, pp. 1323–1325.

[2] Y. H. Kerr, P. Waldteufel, J.-P. Wigneron, J.-M. Martinuzzi, J. Font, and M. Berger, "Soil moisture retrieval from space: The Soil Moisture and Ocean Salinity (SMOS) mission," *IEEE Trans. Geosci. Remote Sens.*, vol. 39, no. 8, pp. 1729–1735, Aug. 2001.

[3] A. B. Tanner and C. T. Swift, "Calibration of a synthetic aperture radiometer," *IEEE Trans. Geosci. Remote Sens.*, vol. 31, no. 1, pp. 257–267, Jan. 1993.

[4] A. Lannes and E. Anterrieu, "Image reconstruction methods for remote sensing by aperture synthesis," in *Proc. IGARSS*, Pasadena, CA, 1994, pp. 2892–2903.
[5] A. Camps, J. Bara, F. Torres, and I. Corbella, "Extension of the clean technique to the microwave imaging of continuous thermal sources by means of aperture synthesis radiometers," *Prog. Electromagn. Res.*, vol. PIER 18, pp. 67–83, 1998.
[6] C. S. Ruf, "Error analysis of image reconstruction by a synthetic aperture interferometric radiometer," *Radio Sci.*, vol. 26, no. 6, pp. 1419–1434, Nov./Dec. 1991.
[7] A. Camps, J. Bara, F. Torres, I. Corbella, and J. Romeu, "Impact of antenna errors on the radiometric accuracy of large aperture synthesis radiometers," *Radio Sci.*, vol. 32, no. 2, pp. 657–668, 1997.
[8] F. Torres, A. Camps, J. Bara, and I. Corbella, "Impact of receiver errors on the radiometric resolution of large two-dimensional aperture synthesis radiometers," *Radio Sci.*, vol. 32, no. 2, pp. 629–641, 1997.
[9] M. A. Goodberlet, "Improved image reconstruction techniques for synthetic aperture radiometers," *IEEE Trans. Geosci. Remote Sens.*, vol. 38, no. 3, pp. 1362–1366, May 2000.
[10] E. Anterrieu, "A resolving matrix approach for synthetic aperture imaging radiometers," *IEEE Trans. Geosci. Remote Sens.*, vol. 42, no. 8, pp. 1649–1656, Aug. 2004.
[11] B. Picard and E. Anterrieu, "Comparison of regularized inversion methods in synthetic aperture imaging radiometry," *IEEE Trans. Geosci. Remote Sens.*, vol. 43, no. 2, pp. 218–224, Feb. 2005.
[12] A. Colliander, S. Tauriainen, T. Auer, J. Kainulainen, J. Uusitalo, M. Toikka, and M. Hallikainen, "MIRAS reference radiometer: A fully polarimetric noise injection radiometer," *IEEE Trans. Geosci. Remote Sens.*, vol. 43, no. 5, pp. 1135–1143, May 2005.
[13] A. R. Thompson, G. W. Swenson, and J. W. Moran, *Interferometry and Synthesis in Radio Astronomy*, 1st ed. Hoboken, NJ: Wiley, 1986.
[14] C. S. Ruf, C. T. Swift, A. B. Tanner, and D. M. LeVine, "Interferometric synthetic aperture radiometry for the remote sensing of the Earth," *IEEE Trans. Geosci. Remote Sens.*, vol. GRS-26, no. 5, pp. 597–611, Sep. 1988.
[15] I. Corbella, N. Duffo, M. Vall-llossera, A. Camps, and F. Torres, "The visibility function in interferometric aperture synthesis radiometry," *IEEE Trans. Geosci. Remote Sens.*, vol. 42, no. 8, pp. 1677–1682, Aug. 2004.
[16] A. Lannes, E. Anterrieu, and K. Bouyoucef, "Fourier interpolation and reconstruction via Shannon-type techniques—Part I: Regularization principle," *J. Mod. Opt.*, vol. 41, no. 8, pp. 1537–1574, Aug. 1994.
[17] ——, "Fourier interpolation and reconstruction via Shannon-type techniques—Part II: Technical developments and applications," *J. Mod. Opt.*, vol. 43, no. 1, pp. 105–138, Jan. 1996.
[18] E. Anterrieu, P. Waldteufel, and A. Lannes, "Apodization functions for 2-D hexagonally sampled synthetic aperture imaging radiometers," *IEEE Trans. Geosci. Remote Sens.*, vol. 40, no. 12, pp. 2531–2542, Dec. 2002.
[19] A. Camps, I. Corbella, M. Vall-llossera, N. Duffo, F. Marcos, F. Martínez-Fadrique, and M. Greiner, "The SMOS end-to-end performance simulator: Description and scientific applications," in *Proc. IGARSS*, Toulouse, France, 2003, pp. 13–15.
[20] A. R. Thompson, B. G. Clark, C. M. Wade, and P. J. Napier, "The very large array," *Astrophys. J., Suppl. Ser.*, vol. 44, pp. 151–167, Oct. 1980.
[21] M. Martin-Neira, S. Ribó, and A. J. Martin-Polegre, "Polarimetric mode of MIRAS," *IEEE Trans. Geosci. Remote Sens.*, vol. 40, no. 8, pp. 1755–1768, Aug. 2002.
[22] P. Waldteufel and G. Caudal, "About off-axis radiometric polarimetric measurements," *IEEE Trans. Geosci. Remote Sens.*, vol. 40, no. 6, pp. 1435–1439, Jun. 2002.

Eric Anterrieu (M'02) was born in Brive, France, in 1965. He received the Engineer and M.S. degrees in solid-state physics from the Institut National des Sciences Appliquées, Toulouse, France, in 1988, and the M.S. and Ph.D. degrees in image reconstruction in astronomy from University Paul Sabatier, Toulouse, in 1989 and 1992, respectively. The subject of his thesis was image reconstruction algorithms for multiple-aperture interferometry.

He is currently with the Signal, Image, and Instrumentation Group in the astrophysics laboratory of the Observatoire Midi-Pyrénées, Toulouse. Since 1993, he has been working as an Engineer of Research in computer science with the Centre National de la Recherche Scientifique. His present research interests now include numerical analysis, image and signal processing with particular emphasis on the SMOS project.